Monthly Notices of the ROYAL ASTRONOMICAL SOCIETY

MNRAS **507,** 116–128 (2021) https://doi.org/10.1093/mnras/stab2048
Advance Access publication 2021 July 21

Modelling neutron star mountains in relativity

Fabian Gittins ★ and Nils Andersson

Mathematical Sciences and STAG Research Centre, University of Southampton, Southampton SO17 1BJ, UK

Accepted 2021 July 14. Received 2021 July 13; in original form 2021 May 13

ABSTRACT

Rapidly spinning, deformed neutron stars have long been considered potential gravitational-wave emitters. However, so far only upper limits on the size of the involved quadrupole deformations have been obtained. For this reason, it is pertinent to ask how large a mountain can be before the neutron star crust fractures. This is the question we consider in this paper, which describes how mountains can be calculated in relativistic gravity. Formally, this is a perturbative calculation that requires a fiducial force to source the mountain. Therefore, we consider three simple examples and increase their deforming amplitudes until the crust yields. We demonstrate how the derived mountains depend on the equation of state by considering a range of models obtained from chiral effective field theory. We find that the largest mountains depend sensitively on both the mechanism that sources them and the nuclear-matter equation of state.

Key words: gravitational waves – stars: neutron.

1 INTRODUCTION

With the recent detections of gravitational waves from binary neutron star mergers (Abbott et al. 2017d, 2020a) and sensitivity improvements of the instruments, there is much anticipation for observing signals from rapidly rotating neutron stars for the first time. Provided a spinning neutron star is deformed in a non-axisymmetric way, it will continuously emit gravitational radiation. These quadrupole deformations are known as *mountains*. Historically, these systems have been of interest since the presence of mountains – resulting in gravitational-wave torques that would spin-down the stars – could play an important role in determining the spin equilibrium for low-mass X-ray binaries (Bildsten 1998; Andersson, Kokkotas & Stergioulas 1999). Thus, providing an explanation for their observed spin distribution, in particular, the lack of sub-millisecond pulsars (Patruno, Haskell & Andersson 2017; Gittins & Andersson 2019).

Although we are yet to be graced with a confirmed gravitational-wave detection of a spinning neutron star, there has been a significant effort to look for signals from individual pulsars (Abbott et al. 2004, 2005b, 2007a, 2008b, 2010, 2017a, c, e, f, 2018b, 2019a, c, d, b, 2021; Abadie et al. 2011a, b; Aasi et al. 2014, 2015a, b; Zhang et al. 2021), accompanied by wide-parameter searches for unknown systems (Abbott et al. 2005a, 2007b, 2008a, 2009, 2016, 2017b, 2018a, 2019b; Abadie et al. 2012; Aasi et al. 2013; Dergachev & Papa 2020, 2021; Steltner et al. 2021). These surveys, through non-detections, have so far only yielded upper limits on the size of possible deformations. Looking at more recent surveys: Abbott et al. (2020b) were able to constrain the ellipticities for the millisecond pulsars PSR J0437−4715 and PSR J0711−6830 to be less than 1×10^{-8}, while Abbott et al. (2021) obtained a constraint of less than 3×10^{-5} for the young pulsar PSR J0537−6910. Indeed, the general trend is that the upper limits of ellipticities of neutron stars are being constrained to lower and lower values. One might think that a pattern is emerging. Furthermore, it has been argued by Woan et al. (2018) that there exists a *minimum* ellipticity for millisecond pulsars of $\epsilon \approx 1 \times 10^{-9}$. In the same vein, Gittins & Andersson (2019) have shown that the features of the spin distribution of accreting millisecond pulsars can be explained by stars with quadrupole deformations of the order of $\epsilon \approx 1 \times 10^{-9}$. It is worth noting that there is only one order of magnitude difference between the smallest established upper limit and 1×10^{-9}, implying the observational constraints are approaching this minimum ellipticity.

The amplitude of the radiation scales with the size of the mountain. Thus, it is a natural question to ask how large a quadrupole deformation can the neutron star crust support? Indeed, this question has been the subject of a number of studies over the past two decades (Ushomirsky, Cutler & Bildsten 2000; Haskell, Jones & Andersson 2006; Johnson-McDaniel & Owen 2013; Gittins, Andersson & Jones 2021). For some time, the standard method to solving this problem has been to follow Ushomirsky et al. (2000), the first to carry out such a maximum-mountain calculation in Newtonian gravity with the aid of the Cowling approximation. By ensuring the crust was maximally strained at every point they obtained the strain field of the crust and could, thus, calculate the mountain it supported. Later, this calculation was generalized to relativistic gravity by Johnson-McDaniel & Owen (2013), while also relaxing the Cowling approximation. However, it has been recently pointed out that there are inconsistencies with all previous studies (Gittins et al. 2021). In particular, there are issues with the boundary conditions of the problem if one is to demand that the crust is maximally strained *at every point*. To this end, Gittins et al. (2021) introduced a novel scheme for

★ E-mail: f.w.r.gittins@soton.ac.uk

calculating neutron star mountains. This scheme requires a fiducial force that sources the mountain, which is contrary to the Ushomirsky et al. (2000) approach, where the force is, in some sense, hidden in the calculation. An important consequence of this work is that the maximum size of a mountain strongly depends on its formation. Therefore, evolutionary calculations will be required in order to make progress on the problem.

The aim of this work is to translate the scheme of Gittins et al. (2021) from Newtonian gravity to relativity – an important step towards realism and greater accuracy which enables us to explore more realistic equations of state. In doing so, we are able to consider how the size of neutron star mountains depend on the description of nuclear matter.

We dedicate Section 2 to a discussion on how one obtains the multipole moments of a body in relativistic gravity and, then, we briefly review the mountain scheme of Gittins et al. (2021). In Section 3, we provide the formalism that describes non-spherical stellar models with and without crusts. This is carried out in a perturbative manner, where the non-spherical, even-parity perturbations are constructed on top of a spherical, fluid background. It is evident from existing results that the mountain problem is well within the linear perturbation regime. We also carefully detail the boundary conditions of the problem. We consider a selection of forces to produce mountains in Section 4 for a sequence of stars with the same realistic equation of state. We also study how the size of the mountains vary with a collection of equations of state from chiral effective field theory in Section 5. To close, we conclude and discuss where future progress will be found for mountain calculations in Section 6.

We use the metric signature $(-, +, +, +)$ and work in geometric units, where $G = c = 1$. We adopt the Einstein summation convention where repeated indices denote a summation. We use early Latin characters a, b, c, ... for space–time indices and later characters i, j, k, ... for spatial indices. We reserve the characters l and m for spherical-harmonic modes. We use primes to denote derivatives with respect to the radial coordinate. Much of the analysis will use perturbation theory, where we denote the Eulerian perturbation of a quantity using δ and the Lagrangian perturbation using Δ. The two are related by $\Delta = \delta + \mathcal{L}_\xi$, where $\mathcal{L}_\xi$ is the Lie derivative along the Lagrangian displacement vector, ξ^a (Friedman & Schutz 1978).

2 CALCULATING MOUNTAINS

2.1 Multipole moments in relativity

There is freedom in how one chooses to define the multipole moments. However, we must be consistent in order to compare previous Newtonian calculations (Ushomirsky et al. 2000; Haskell et al. 2006; Gittins et al. 2021) with this calculation in relativity. The quadrupole we obtain matches the definition used in the relativistic calculation of Johnson-McDaniel & Owen (2013).

We treat multipole moments as departures from perfect spherical symmetry. In Newtonian gravity, consider a star that is deformed away from sphericity according to the mass-density perturbation, $\delta\rho$. The multipole moments of the star are then defined as

$$Q_{lm} \equiv \int_V \delta\rho r^l Y^*_{lm} \mathrm{d}V, \tag{1}$$

where (l, m) is the order of the spherical-harmonic mode, $Y_{lm}(\theta, \phi)$, and the star denotes a complex conjugate. One is free to decompose the angular behaviour of an arbitrary function using spherical harmonics, e.g. the perturbation of the mass density may be written as $\delta\rho(r, \theta, \phi) = \sum_{l=0}^{\infty} \sum_{m=-l}^{l} \delta\rho_{lm}(r) Y_{lm}(\theta, \phi)$. Therefore, (1) can be expressed as

$$Q_{lm} = \int_0^R \delta\rho_{lm}(r) r^{l+2} \mathrm{d}r, \tag{2}$$

where R is the radius of the background spherical star. By combining the perturbed Poisson's equation,

$$\nabla^2 \delta\Phi = 4\pi\delta\rho, \tag{3}$$

where $\delta\Phi$ is the perturbation of the gravitational potential with boundary conditions (assuming that the density vanishes at the star's surface)

$$\delta\Phi_{lm}(0) = 0, \qquad R\delta\Phi'_{lm}(R) = -(l+1)\delta\Phi_{lm}(R), \tag{4}$$

with the multipole definition (2), one can show, for $r \geq R$,

$$\delta\Phi_{lm}(r) = -\frac{4\pi}{2l+1} \frac{Q_{lm}}{r^{l+1}}. \tag{5}$$

Therefore, provided one is able to find the perturbed potential in the exterior of the star, one can straightforwardly read off the multipole moments, Q_{lm}.

In general relativity, the space–time metric, g_{ab}, replaces the Newtonian potential, Φ. In the far-field exterior of the star, $r \gg R$, one obtains the Newtonian limit,

$$-\frac{1 + g_{tt}}{2} = \Phi + \chi, \tag{6}$$

where χ is the corresponding potential to the force that sources the deformation. It should be noted that the deforming potential, χ, is necessary in order to induce a non-spherical deformation (Gittins et al. 2021). Equation (6) illustrates an important point. Although in Newtonian

gravity one can analyse the gravitational and deforming potentials separately, such a neat decoupling does not necessarily exist in relativity. In relativity, one has the metric that accounts for all the potentials acting on the body. For this reason, in some cases, it is not possible to disentangle the separate potentials from the metric and ambiguities arise.[1] However, no ambiguities occur when one considers pure multipoles of order l. Indeed, we will focus on pure multipoles of order (l, m). In this case, for $r \geq R$, we have (cf. a variation of 6)

$$-\frac{h_{tt}}{2} = -\frac{4\pi}{2l+1} B_l(r) \frac{Q_{lm} Y_{lm}}{r^{l+1}} + \chi_{lm}(r) Y_{lm}, \tag{7}$$

where $h_{ab} \equiv \delta g_{ab}$ is the linearized metric, $B_l(r)$ is a function that goes to unity in the Newtonian limit (this is given as B_1 in table I of Binnington & Poisson 2009) and we treat the deforming potential, χ, as a first-order parameter. Equation (7) is obtained by looking for a solution to the perturbed Einstein equations in the exterior of the star.[2] (Note that χ need not be a solution to the vacuum Einstein equations. It simply corresponds to a force that deforms the shape of the star.) Since we are interested in calculating the quadrupole moment, Q_{22}, it will be sufficient for this work to focus on the $(l, m) = (2, 2)$ mode, so we will henceforth neglect the mode subscript on the perturbation variables.

2.2 Mountain scheme

We briefly summarize the method for calculating mountains introduced by Gittins et al. (2021). Contrary to the Ushomirsky et al. (2000) approach that begins with the strain, the scheme of Gittins et al. (2021) instead requires a description of the deforming force.

Consider two stars: (i) a purely fluid star (star A) and (ii) a star with a crust (star B). Both stars begin with the same spherical shape and the crust of star B is relaxed in this shape. The two stars are subjected to the same $(l, m) = (2, 2)$ force that deforms them into non-spherical shapes. As star B is deformed, strain is built up in the crust as the stresses resist the change in shape. The two stars, supported by the same force, are then subtracted from one another to cancel out the force.[3] This procedure provides the perturbation quantities that connect a spherical background to a star with a mountain supported by elastic stresses. Provided a description of the deforming force, one can then calculate all the relevant information about the star with a mountain. It was shown in Gittins et al. (2021) how this scheme does, in fact, produce the same non-spherical star with a mountain as considered in previous mountain calculations. The advantage to this new scheme is that one has full control over the boundary conditions of the problem. The disadvantage is the necessity to prescribe the force, which should ideally take into account some (presently) poorly understood aspects of neutron star physics.

With this scheme for computing mountains, there is a natural way to obtain the largest quadrupole for a given force: the amplitude of the force is increased until a point in the crust of star B reaches breaking strain. The obtained mountains can then be readily compared with previous estimates.

Gittins et al. (2021) considered several examples for the form of the deforming force and found that their mountains were between a factor of a few to two orders of magnitude smaller than the results from previous maximum-mountain calculations. The reason for this difference lies in the fact that the crust breaks at a point in the scheme of Gittins et al. (2021), rather than throughout the crust.

3 STELLAR MODELS

In order to implement the scheme described in Section 2.2, we need to construct pairs of relativistic stellar models with and without crusts. We will focus on non-rotating stars and assume that stars A and B differ to a spherically symmetric star in a perturbative way. This enables us to generate the stars through perturbations on a spherical background. We use the static perturbation formalism provided in Gittins, Andersson & Pereira (2020) to build the stars.

The fact that star B is relaxed in a spherical shape provides significant simplification: the crust manifests itself only at the linear perturbation level. In order to model the crust, we will assume that it is well approximated as an elastic solid. Star B will be partitioned into three layers: a fluid core, an elastic crust, and a fluid ocean.

3.1 Background

In general relativity, a stellar configuration – characterized by a space–time metric, g_{ab}, with energy density ε and isotropic pressure p as measured by an observer with four-velocity u^a – is a solution $(\varepsilon, p, u^a, g_{ab})$ to the Einstein field equations,

$$G_a{}^b = 8\pi T_a{}^b, \tag{8}$$

where $G_a{}^b$ is the Einstein tensor and $T_a{}^b$ is the stress-energy tensor, supplemented by an equation of state,

$$p = p(\varepsilon), \tag{9}$$

[1]To be specific, ambiguities occur when different potentials mix in powers of r. Much of the work concerning separating multiple gravitational effects in relativity has come from studies on tidal deformations (see, e.g., Gralla 2018).

[2]We note that (7) differs slightly, by a constant factor, from equivalent expressions in the tidal-deformation literature (see, e.g., equation 1 in Hinderer 2008). This is due to the different convention for defining the multipole moments originating from Thorne (1980) [cf. their equation (5.27a) with (1)].

[3]Note that the two stars that are subtracted from one another are called star A and star C in Gittins et al. (2021).

which we have assumed to be barotropic. The equilibrium of a non-rotating, spherically symmetric, fluid star is described by the line element of the form,

$$ds^2 = g_{ab}dx^a dx^b = -e^{\nu}dt^2 + e^{\lambda}dr^2 + r^2(d\theta^2 + \sin^2\theta\, d\phi^2), \tag{10}$$

where ν and λ are metric functions, with the stress-energy tensor,

$$T_a{}^b = (\varepsilon + p)u_a u^b + p\delta_a{}^b = \varepsilon u_a u^b + p \perp_a{}^b, \tag{11}$$

appropriate for perfect fluids, where $\perp_a{}^b \equiv u_a u^b + \delta_a{}^b$ is the projection operator orthogonal to the four-velocity, u^a, which we will use later. Since the star is spherically symmetric, all quantities are solely functions of the radial coordinate, r. It is convenient to choose an observer at rest with the fluid. As the fluid is static, the four-velocity (which must be normalized, $u^a u_a = -1$) may be simply given by

$$u^t = e^{-\nu/2}, \qquad u^i = 0. \tag{12}$$

Putting this information into the field equations (8) provides the relativistic equations of stellar structure for a non-rotating, fluid star:

$$m' = 4\pi r^2 \varepsilon, \tag{13a}$$

$$p' = -\frac{1}{2}(\varepsilon + p)\nu' \tag{13b}$$

and

$$\nu' = \frac{2(m + 4\pi r^3 p)}{r(r - 2m)}, \tag{13c}$$

where $m(r) = r[1 - e^{-\lambda(r)}]/2$ is the gravitational mass enclosed in r. Along with the equation of state (9), these structure equations describe the spherical background.

3.2 Fluid perturbations

To generate star A and the fluid regions of star B, we must consider fluid perturbations. The perturbations are a solution ($\delta\varepsilon$, δp, δu^a, h_{ab}) to the linearized Einstein equations,

$$\delta G_a{}^b = 8\pi \delta T_a{}^b. \tag{14}$$

As the matter is barotropic, we have

$$\delta p = c_s^2 \delta\varepsilon, \tag{15}$$

where $c_s^2 \equiv dp/d\varepsilon$ is the squared sound speed. Since we intend to build stars with quadrupolar deformations, we work in the Regge–Wheeler gauge (Regge & Wheeler 1957) specialized to static, even-parity perturbations. This gives the linearized metric,

$$h_{ab} = \begin{pmatrix} e^{\nu}H_0 & H_1 & 0 & 0 \\ H_1 & e^{\lambda}H_2 & 0 & 0 \\ 0 & 0 & r^2 K & 0 \\ 0 & 0 & 0 & r^2\sin^2\theta\, K \end{pmatrix} Y_{lm}, \tag{16}$$

where $H_0(r)$, $H_1(r)$, $H_2(r)$ and $K(r)$ are the perturbed metric functions. The perturbations of the metric are coupled to the perturbations of the stress-energy tensor, which for fluid perturbations are given by (cf. a perturbation of 11)

$$\delta T_a{}^b = (\delta\varepsilon + \delta p)u_a u^b + \delta p \delta_a{}^b + (\varepsilon + p)\left(\delta u_a u^b + u_a \delta u^b\right). \tag{17}$$

The perturbed quantities are to be expanded using spherical harmonics. The linearized four-velocity for static, even-parity perturbations is

$$\delta u^t = \frac{1}{2}e^{-\nu/2}H_0 Y_{lm}, \qquad \delta u^i = 0. \tag{18}$$

The perturbed Einstein equations (14) for a fluid yield the following system of equations:

$$H_0'' + \left(\frac{2}{r} + \frac{\nu' - \lambda'}{2}\right)H_0' + \left\{\frac{2}{r^2} - [2 + l(l+1)]\frac{e^{\lambda}}{r^2} + \frac{4\nu' + 2\lambda'}{r} - \nu'^2\right\}H_0 = -8\pi e^{\lambda}(\delta\varepsilon + \delta p), \tag{19a}$$

$$\delta p = \frac{e^{-\lambda}(\nu' + \lambda')}{16\pi r}H_0, \tag{19b}$$

$$H_1 = 0, \tag{19c}$$

$$H_2 = H_0 \tag{19d}$$

and

$$[l(l+1)-2]e^{\lambda}K = r^2\nu' H_0' + [l(l+1)e^{\lambda} - 2 - r(\nu'+\lambda') + r^2\nu'^2]H_0. \tag{19e}$$

Equations (19) provide the necessary information to compute static, even-parity perturbations in the fluid regions of a star. At this point, we should note that the perturbation equations in this form do not necessarily include the force that sources the deformation – unless the force satisfies the relativistic analogue to Laplace's equation. In this situation, which is effectively the tidal problem (see, e.g., Hinderer 2008), the perturbed metric function, H_0, contains both the gravitational and tidal potentials. When we consider examples, we will discuss how one may include the force.

3.3 Elastic perturbations

In stellar perturbation theory, it is traditional to work with the Lagrangian displacement vector, ξ^a, that connects fluid elements in the perturbed configuration to their positions in the background. Due to the static nature of the problem, one is unable to calculate the displacement for the fluid perturbations. However, this is different in elastic material. We will define the displacement vector appropriate for static, even-parity perturbations,

$$\xi^a = \begin{bmatrix} 0 \\ r^{-1}W \\ r^{-2}V\partial_\theta \\ (r\sin\theta)^{-2}V\partial_\phi \end{bmatrix} Y_{lm}, \tag{20}$$

where the functions $W(r)$ and $V(r)$ capture the radial and tangential displacements, respectively.

In order to compute the crust of star B, we must consider perturbations of an elastic solid. For an elastic material with shear modulus μ, the perturbed anisotropic stress tensor is (Andersson et al. 2019)

$$\Delta\pi_{ab} = -2\mu\Delta s_{ab}, \tag{21}$$

where the perturbed strain tensor, Δs_{ab}, is given by

$$2\Delta s_{ab} = \left(\perp^c{}_a\perp^d{}_a - \frac{1}{3}\perp_{ab}\perp^{cd}\right)\Delta g_{cd} \tag{22}$$

and the perturbation to the metric is $\Delta g_{ab} = h_{ab} + \nabla_a\xi_b + \nabla_b\xi_a$. For an unstrained background, we find

$$\delta\pi_a{}^b = -\mu\left(\perp^c{}_a\perp^{db} - \frac{1}{3}\perp_a{}^b\perp^{cd}\right)\Delta g_{cd}. \tag{23}$$

In the elastic crust, the linearized stress-energy tensor includes the fluid contribution (17) summed with the elastic stress tensor (23). For the application of the boundary conditions, it is convenient to define the following variables that are related to the traction components:

$$T_1 Y_{lm} \equiv r^2\delta\pi_r{}^r = \frac{2\mu}{3}\left[r^2(K-H_2) - l(l+1)V - 2rW' + (4-r\lambda')W\right]Y_{lm} \tag{24a}$$

and

$$T_2\partial_\theta Y_{lm} \equiv r^3\delta\pi_r{}^\theta = -\mu(rV' - 2V + e^{\lambda}W)\partial_\theta Y_{lm}. \tag{24b}$$

Using this information in the perturbed Einstein field equations (14) provides the elastic perturbation equations:

$$H_0'' + \left(\frac{2}{r} + \frac{\nu'-\lambda'}{2}\right)H_0' + \left\{\frac{2}{r^2} - [2+l(l+1)]\frac{e^{\lambda}}{r^2} + \frac{3\nu'+\lambda'}{r} - \nu'^2\right\}H_0 = -8\pi\Bigg[e^{\lambda}(3\delta p + \delta\varepsilon) + 2\nu'(\mu V)' + 8\left(\frac{1-e^{\lambda}}{r^2} + \frac{2\nu'+\lambda'}{2r} - \frac{1}{4}\nu'^2\right)\mu V + \frac{2\nu'}{r}T_2\Bigg], \tag{25a}$$

$$K' = H_0' + \nu' H_0 + \frac{16\pi}{r}(2+r\nu')\mu V - \frac{16\pi}{r}T_2, \tag{25b}$$

$$W' - \left(\frac{2}{r} - \frac{\lambda'}{2}\right)W = \frac{1}{2}r(K-H_0) - \left[16\pi r\mu + \frac{l(l+1)}{2r}\right]V - \frac{3}{4r\mu}T_1, \tag{25c}$$

$$V' - \frac{2}{r}V = -\frac{e^{\lambda}}{r}W - \frac{1}{r\mu}T_2, \tag{25d}$$

$$T_2' + \left(\frac{\nu'-\lambda'}{2} + \frac{1}{r}\right)T_2 = -e^{\lambda}r\delta p + \frac{\nu'+\lambda'}{16\pi}H_0 + \frac{e^{\lambda}}{r}[2-l(l+1)]\mu V + \frac{e^{\lambda}}{2r}T_1, \tag{25e}$$

$$16\pi e^{\lambda}r^2\delta p = r^2\nu' H_0' + [l(l+1)e^{\lambda} - 2 + r^2\nu'^2]H_0 + [2-l(l+1)]e^{\lambda}K + 16\pi r^2\nu'^2\mu V - 16\pi e^{\lambda}T_1 - 16\pi(2+r\nu')T_2, \tag{25f}$$

$$\frac{3}{4\mu}T_1 = \frac{r^2}{(\varepsilon+p)}\delta\varepsilon + \frac{3}{2}r^2K - \frac{3}{2}l(l+1)V + \left(3 - \frac{r\nu'}{2c_s^2}\right)W, \tag{25g}$$

$$H_1 = 0 \tag{25h}$$

and

$$H_2 = H_0 + 32\pi\mu V. \tag{25i}$$

Equations (25) form a coupled system of equations that describe the static, even-parity perturbations in the elastic crust. It is straightforward to show that, when the shear modulus vanishes, equations (25) reduce to the perturbation equations (19) for the fluid.

3.4 Boundary conditions

To solve the perturbation equations, we need to consider the boundary conditions of the problem. At the centre of the star, the solution must be regular,

$$H_0(0) = 0. \tag{26}$$

However, as the structure equations are singular at the origin, we must begin integrating at small r. Regularity provides the initial condition,

$$H_0(r) = a_0 r^l [1 + \mathcal{O}(r^2)], \tag{27}$$

where a_0 is a constant that depends on the amplitude of the perturbations.

There are two fluid–elastic interfaces in star B: the core–crust and crust–ocean boundaries. Because the star is unstrained in the background, the background quantities will be continuous across these boundaries. However, should the equation of state involve discontinuities at the phase transitions, these would need to be accounted for (see, e.g., Pereira et al. 2020).

In order to determine how the perturbed variables behave at a boundary, one must inspect the first and second fundamental forms, which both must be continuous at the interfaces (Finn 1990; Penner et al. 2011; Gittins et al. 2020). From this analysis, one finds that the functions H_0, K and W must be continuous, along with the traction, which has components, $(T_1 + r^2\delta p)$ and T_2. We assume the shear modulus has a finite value throughout the crust and therefore is discontinuous at a fluid–elastic boundary, since a fluid has a vanishing shear modulus. This is an important, yet subtle, point as in the alternative case, where the shear modulus approaches zero at an interface, one finds that the tangential traction condition is trivially satisfied and there are insufficient boundary conditions to solve the problem.

Towards the surface of both stars A and B, there is a fluid ocean. In a fluid, all perturbed metric functions and their derivatives are continuous. Therefore, the interior solution will match smoothly to the exterior. In the vacuum, we find that (19a) reduces to

$$H_0'' + \left(\frac{2}{r} - \lambda'\right) H_0' - \left[l(l+1)\frac{e^{\lambda}}{r^2} + \lambda'^2\right] H_0 = 0. \tag{28}$$

This is the relativistic analogue of the linearized Laplace's equation for non-radial perturbations. The solution to (28) may be expressed in terms of associated Legendre polynomials and for quadrupolar ($l = 2$) perturbations is

$$H_0(r) = c_1 \left(\frac{r}{M}\right)^2 \left(1 - \frac{2M}{r}\right) \left[-\frac{M(M-r)(2M^2+6Mr-3r^2)}{r^2(2M-r)^2} + \frac{3}{2}\ln\left(\frac{r}{r-2M}\right)\right] + 3c_2 \left(\frac{r}{M}\right)^2 \left(1 - \frac{2M}{r}\right), \tag{29}$$

where $M \equiv m(R)$ is the total gravitational mass of the background and c_1 and c_2 are constants. From (29), we observe two solutions to the relativistic Laplace's equation: a decreasing solution with c_1, which is associated with the gravitational potential of the star, and an increasing solution with c_2, which may be associated with the tidal potential (see, e.g., Hinderer 2008). For other applications, one can assume $c_2 = 0$ and H_0 only contains the star's potential. By comparing (7) and (29), we identify

$$Q_{2m} = \frac{M^3 c_1}{\pi}, \tag{30}$$

in agreement with equation (41) in Johnson-McDaniel & Owen (2013). Thus, one can obtain the quadrupole moment by identifying the decreasing solution in H_0.

In the fluid regions, one must solve for (H_0', H_0) using equations (19). In the elastic crust of star B, the perturbations are governed by equations (25) with variables $(H_0', H_0, K, W, V, T_2)$. Equation (27) provides the initial boundary condition in the fluid core. The crust of star B presents a boundary-value problem with six boundary conditions: continuity of H_0 and K at the core–crust interface and continuity of the traction at both interfaces. (The calculation of this boundary-value problem is described in detail in Appendix B of Gittins et al. 2020.) At the surface, the solution must match (29).

4 THE SOURCE OF THE DEFORMATION

For the pressure–density relation, we first use the analytic BSk24 equation of state (Pearson et al. 2018) for the high-density regions ($\varepsilon > 1 \times 10^6\,\mathrm{g\,cm^{-3}}$) of the star and the Douchin & Haensel (2001) table for the low-density regions ($\varepsilon \leq 1 \times 10^6\,\mathrm{g\,cm^{-3}}$). In the crust, we need to prescribe the shear-modulus profile. We use the Ogata & Ichimaru (1990) result,

$$\mu = 0.1994 \left(\frac{4\pi}{3}\right)^{1/3} \left(\frac{1 - X_{\mathrm{n}}}{A} n_{\mathrm{b}}\right)^{4/3} (eZ)^2, \tag{31}$$

where X_n is the free neutron fraction, A and Z are the atomic and proton numbers, respectively, n_b is the baryon number density, and e is the fundamental electric charge. We neglect any phase transitions in the crust (as they would significantly complicate the calculation). For the nuclear-matter parameters, we use the BSk24 results for the inner crust and the HFB-24 model (Goriely, Chamel & Pearson 2013) along with the experimental data from the 2016 Atomic Mass Evaluation (Wang et al. 2017) for the outer crust (see table 4 in Pearson et al. 2018). The location of the core–crust transition is given by the BSk24 results and the crust–ocean transition is taken to be the lowest density in the outer-crust model. The complexity of this prescription is due to our attempt to use a consistent model for the neutron star physics.

We consider three sources for the perturbations: (i) a deforming potential that is a solution to the relativistic Laplace's equation, (ii) a thermal pressure perturbationT and (iii) a thermal pressure perturbation that only acts outside the core. Sources (i) and (ii) are the relativistic equivalents of two forces we considered in our Newtonian calculation (Gittins et al. 2021). In reality, the fiducial force will depend on the evolutionary history of the star. Since this is a complex problem (beyond the scope of this work), the examples we consider are indicative in nature and should serve as illustrations of how one can calculate mountains using this scheme. The forces we use should not be interpreted as having an explicit link with the neutron star physics. To calculate the mountains for each example, we follow the Gittins et al. (2021) scheme outlined in Section 2.2. The perturbations are normalized by ensuring star B reaches breaking strain at a point in its crust. In practice, this means we take the point in the crust where the strain is greatest and set that to breaking strain. To obtain the perturbation amplitude, we use the von Mises criterion. In the formalism of Andersson et al. (2019), the von Mises strain for a star with an unstrained background is

$$\Theta = \sqrt{\frac{3}{2}\Delta s_{ab}\Delta s^{ab}}. \tag{32}$$

The von Mises criterion states that a point in the crust fractures when the von Mises strain reaches the threshold, $\Theta \geq \Theta^{\rm break}$, at some point. For $(l, m) = (2, 2)$ perturbations, we have the explicit expression

$$\Theta^2 = \frac{45}{512\pi}\left\{\sin^2\theta\left[3\sin^2\theta\cos^2 2\phi\left(\frac{T_1}{r^2\mu}\right)^2 + 4e^{-\lambda}(3+\cos 2\theta - 2\sin^2\theta\cos 4\phi)\left(\frac{T_2}{r^2\mu}\right)^2\right]\right.$$
$$\left. + (35 + 28\cos 2\theta + \cos 4\theta + 8\sin^4\theta\cos 4\phi)\left(\frac{V}{r^2}\right)^2\right\}. \tag{33}$$

Following the results of molecular-dynamics simulations by Horowitz & Kadau (2009), we take the breaking strain to be $\Theta^{\rm break} = 0.1$. Other estimates for the magnitude of the breaking strain include Baiko & Chugunov (2018) who obtained the smaller value of $\Theta^{\rm break} = 0.04$. However, as was the case for previous maximum-mountain calculations, our results are linear in the breaking strain. Thus, a smaller breaking strain would result in less pronounced mountains.

For our results, we will report, alongside the quadrupole moment, the fiducial ellipticity,

$$\epsilon = \sqrt{\frac{8\pi}{15}}\frac{Q_{22}}{I_{zz}}, \tag{34}$$

where I_{zz} is the principal stellar moment of inertia, taken to be $I_{zz} = 1 \times 10^{45}\,{\rm g\,cm^2}$. It is worth emphasizing that the fiducial ellipticity does not perfectly correspond to the star's actual deformation. However, the principal moment of inertia is not expected to differ from the fiducial value by more than a factor of a few. We include the fiducial ellipticity to streamline comparison with observational results. Our results for the different forces are summarized in Fig. 1.

4.1 A solution to the relativistic Laplace's equation

The relativistic Laplace's equation is given by the vacuum Einstein equations (28). A common example of a solution to these equations is the tidal potential. In this situation, the perturbed metric function, H_0, has two contributions: the gravitational potential of the deformed star and the tidal potential of the companion. From (29), we can calculate the constants, c_1 and c_2, using H_0 and H_0' in the exterior:

$$c_1 = \frac{r(r-2M)}{8M^3}\left[r(2M-r)H_0'(r) + 2(r-M)H_0(r)\right] \tag{35a}$$

and

$$c_2 = \frac{1}{48M^3r(2M-r)}\left\{-2M[r(4M^4 + 6M^3r - 22M^2r^2 + 15Mr^3 - 3r^4)H_0'(r) + 2(2M^4 - 2M^3r + 13M^2r^2 - 12Mr^3 + 3r^4)H_0(r)]\right.$$
$$\left. + 3r^2(r-2M)^2[r(2M-r)H_0'(r) + 2(r-M)H_0(r)]\ln\left(\frac{r}{r-2M}\right)\right\}. \tag{35b}$$

At the surface, H_0 and its derivative are continuous, so we can use their values at this point to calculate the force amplitude (35b) and the quadrupole (30).

Therefore, we compute stars A and B using the fluid (19) and elastic perturbations equations (25) for $(l, m) = (2, 2)$ perturbations. At the surface, we obtain the amplitude of the force from (35b) and increase its amplitude until a point in the crust breaks according to (33). Then, once the two stars are normalized to the same force, we calculate the quadrupole moment with (30) and (35a).

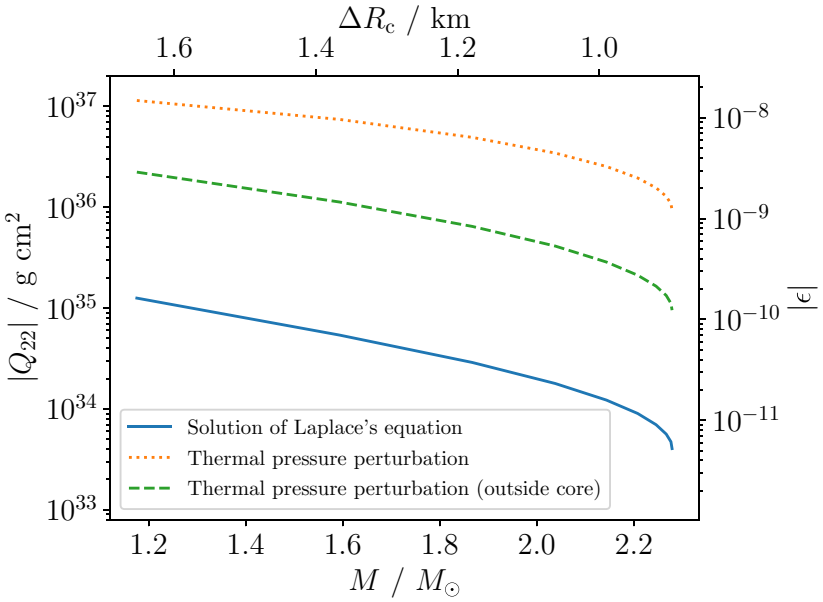

Figure 1. The maximum quadrupole and ellipticity due to the different forces as functions of stellar mass and crustal thickness, ΔR_c. We show results for the force corresponding to the solution of Laplace's equation (solid blue line), the thermal pressure perturbation (dotted orange line), and the thermal pressure perturbation that acts outside the core (dashed green line).

Fig. 1 shows the maximum deformations with such a force for varying stellar mass. In the equivalent Newtonian case, for a star with $M = 1.4\,\mathrm{M}_\odot$, $R = 10\,\mathrm{km}$, we found $Q_{22} = 1.7e37\,\mathrm{g\,cm^2}$, $\epsilon = 2.2 \times 10^{-8}$ (Gittins et al. 2021). We see that the corresponding maximum deformation for an $M = 1.4\,\mathrm{M}_\odot$ star is two orders of magnitude lower. This suppression has two contributions. In going from Newtonian to relativistic gravity, the maximum size of the quadrupole that a crust can support decreases. This suppression was observed by Johnson-McDaniel & Owen (2013) in their relativistic calculation and has also been seen in tidal- (Hinderer 2008; Binnington & Poisson 2009; Damour & Nagar 2009; Hinderer et al. 2010) and magnetic-deformation calculations (Ioka & Sasaki 2004; Ciolfi, Ferrari & Gualtieri 2010; Frieben & Rezzolla 2012; Yoshida, Kiuchi & Shibata 2012). This behaviour has been attributed to the stiffness of the external, vacuum space–time, that suppresses the quadrupole in the matching at the stellar surface (Johnson-McDaniel & Owen 2013).

The second effect comes from the equation of state. Focusing on the role of the matter model in our calculations, we found that the point where the strain was the largest for all the forces we considered was the top of the crust. This is where the crust yields which is consistent with previous calculations of neutron star crusts (Gittins et al. 2020, 2021). In Fig. 2, we compare the shear-modulus profile used in this work with the linear model used in our Newtonian calculation (Gittins et al. 2021). Although the linear model appears to be a reasonable approximation to the more realistic model, there are key areas where the two differ. Of particular importance to the maximum-mountain calculation, the realistic shear-modulus profile is significantly weaker in the lower density outer crust (approximately an order of magnitude smaller at the top of the crust). This plays a pivotal role in determining the size of the mountains that the crust can support as the breaking strain scales with the shear modulus.

Our results are at least two to three orders of magnitude smaller than the mountains obtained by Johnson-McDaniel & Owen (2013). As was noted by Gittins et al. (2021), the fact that our scheme produces smaller mountains than calculated in previous work is not particularly surprising. Indeed, the very nature of the Ushomirsky et al. (2000) approach (that Johnson-McDaniel & Owen 2013 follow) is to ensure that the *entire* crust is at breaking strain, whereas in our scheme (in order to correctly satisfy the boundary conditions of the problem) breaking strain is reached at a point. Clearly, the size of the mountains depends on the force, so it is natural to explore different choices to see if we can obtain larger deformations. We will go on to consider a couple of other examples.

4.2 A thermal pressure perturbation

The next source for the perturbations enters the problem in the same way as a thermal pressure. For this case, we assume that the pressure has a thermal component of the form (Gittins et al. 2021),

$$\delta p_{\mathrm{th}} = \frac{k_{\mathrm{B}}\varepsilon}{m_{\mathrm{u}}}\delta T, \tag{36}$$

where k_{B} is the Boltzmann constant, m_{u} is the atomic mass unit and δT is the perturbation to the temperature. Since the temperature perturbation must be regular at the centre of the star, we will assume its radial dependence is given by

$$\delta T(r) = \left(\frac{r}{R}\right)^2 \delta T(R). \tag{37}$$

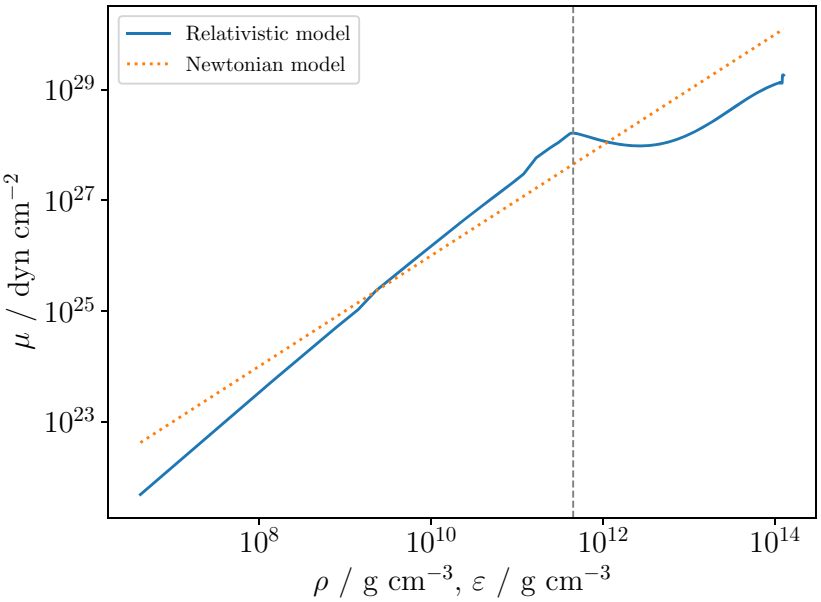

Figure 2. The shear modulus as a function of energy density, ε, for the model of the crust in this relativistic calculation (solid blue line) and as a function of mass density, ρ, for the linear model used in the Newtonian calculation (dotted orange line). We show the density at which the crust transitions from the inner crust to the outer crust (known as neutron drip; vertical dashed grey line).

To incorporate this force into the perturbation equations (19) and (25), they must be adjusted by $\delta p \to \delta p + \delta p_{\rm th}$. In this case, H_0 corresponds solely to the gravitational potential of the star.

For this example, the amplitude a_0 in (27) is connected to the magnitude of the temperature perturbation. It is constrained by ensuring the function H_0 matches the exterior solution (29) with $c_2 = 0$. This boundary condition can be expressed as

$$-\frac{1}{2}(R-2M)H_0'(R) = \left\{-1+\frac{M}{R}-\frac{8M^5}{2MR(M-R)(2M^2+6MR-3R^2)+3R^3(R-2M)^2\ln[(R-2M)/R]}\right\}H_0(R), \tag{38}$$

which is the relativistic analogue (for $l = 2$ perturbations) of the Newtonian boundary condition at the surface in (4). The temperature perturbation, $\delta T(R)$, is then increased until a point in the crust breaks.[4]

The maximum mountains built using this force are shown in Fig. 1. Compared to the solution to the relativistic Laplace's equation, the thermal pressure perturbation produces mountains approximately two orders of magnitude larger. As we saw in the Newtonian calculation (Gittins et al. 2021), this illustrates that the size of the mountains that can be built are highly dependent on their formation history.

For comparison, the corresponding force in our Newtonian calculation gave $Q_{22} = 4.0 \times 10^{38}\,\mathrm{g\,cm^2}$, $\epsilon = 5.2 \times 10^{-7}$. Hence, the suppression for the thermal pressure is weaker than in the previous example.

We also considered the situation where the top of the crust was moved to neutron drip in order to assess the impact of removing the weaker regions of the crust. In this case, for an $M = 1.4\,\mathrm{M}_\odot$ star, we obtained $Q_{22} = 5.9 \times 10^{38}\,\mathrm{g\,cm^2}$, $\epsilon = 7.7 \times 10^{-7}$, which is even larger than what was obtained in the Newtonian calculation. This is not particularly surprising since we only focus on the inner crust, which is orders of magnitude stronger in the shear modulus than most of the outer crust (see Fig. 2). We also found that the crust no longer yielded at the top. This illustrates the role the shear modulus plays in supporting the mountains.

4.3 A thermal pressure perturbation outside the core

We also consider the case where the thermal pressure perturbation does not reach into the core. One could imagine a scenario where the surface of the neutron star is heated and this heating does not penetrate to the core. We will assume that the thermal pressure has a finite value at the base of the crust and exists in the crust and ocean. We use the same form for the temperature perturbation (37).

Due to the specificity of this force, one must be careful in setting up the calculation. Since the core is unperturbed, we will assume $H_0(r_{\rm base}) = W(r_{\rm base}) = 0$, where $r_{\rm base}$ denotes the position of the base of the crust. Because the force suddenly appears at the base, we assume that $H_0'(r_{\rm base})$ is non-zero. For the fluid star (star A), this is sufficient to calculate the mountains. The precise value of H_0' at the base is determined by ensuring the surface boundary condition (38) is satisfied.

For the star with a crust (star B), we need to pay attention to the traction conditions. Since H_0' needed to have a finite value at the base of the crust in the fluid star, we effectively violated the radial traction condition (cf. A17 in Gittins et al. 2020). However, we can still use the

[4]For a canonical $M = 1.4\,\mathrm{M}_\odot$ star, we found the crust breaks when $\delta T(R) = 9.4 \times 10^4\,\mathrm{K}$. The temperature reported here is not a physical temperature perturbation the star is subjected to, noting that the background is at zero temperature. It is simply a source term for the pressure perturbation (36).

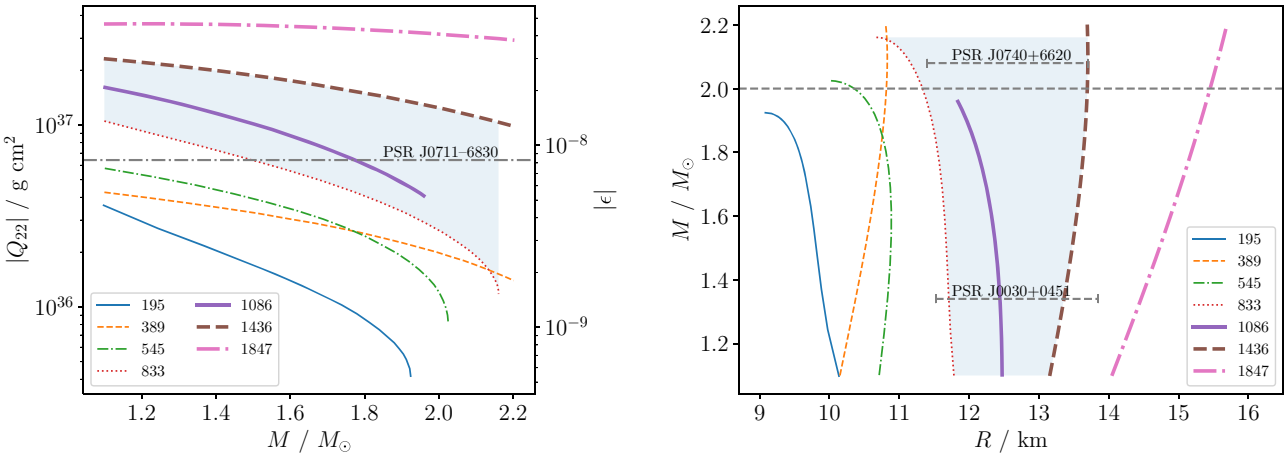

Figure 3. The maximum quadrupole and ellipticity due to thermal pressure perturbations as functions of stellar mass for different chiral effective-field-theory equation-of-state models (left-hand panel) and the corresponding mass–radius diagram traced out by the background stellar models (right-hand panel). To compare with observational constraints, we indicate the $M = 2\,\mathrm{M}_\odot$ constraint (middle dashed grey line) and the range of radii $11.52 \leq R/\mathrm{km} \leq 13.85$ (bottom dashed grey line) and $11.4 \leq R/\mathrm{km} \leq 13.7$ (top dashed grey line) measured for PSR J0030+0451 and PSR J0740+6620, respectively, in the right-hand panel. We shade the region between the two models 833 and 1436 that (roughly) satisfy the constraints to give an indication of the range of possible maximum deformations for this force. On the left-hand panel, we indicate the upper limit on the ellipticity of PSR J0711–6830, $\epsilon < 8.3 \times 10^{-9}$ (dash–dotted grey line). The equations of state are indexed according to their radii for an $M = 1.4\,\mathrm{M}_\odot$ star. All stellar models considered are stable to radial perturbations.

tangential traction condition to demand $T_2(r_{\mathrm{base}}) = 0$. This leaves two free values, $K(r_{\mathrm{base}})$ and $V(r_{\mathrm{base}})$. At the top of the crust we still impose both traction conditions, which constrains $K(r_{\mathrm{base}})$ and $V(r_{\mathrm{base}})$ and, thus, the problem is well posed. As was the case for the fluid star, $H_0'(r_{\mathrm{base}})$ is constrained via (38).

We plot the maximum mountains for this case in Fig. 1. As compared to the thermal pressure that acts throughout the star, the mountains produced in this example are approximately an order of magnitude smaller.

In summary, we have seen with all our examples in Fig. 1 that the maximum deformations the crust can sustain are small. Nevertheless, it is interesting to note that our results are, in principle, large enough to be consistent with the minimum deformation argument of Woan et al. (2018) and the quadrupoles that can describe the accreting millisecond pulsar population (Gittins & Andersson 2019).

5 DEPENDENCE ON THE EQUATION OF STATE

As the calculation is done in full general relativity, we have the opportunity to assess the impact of the equation of state. To do this, we explore a subset of the chiral effective-field-theory models combined with a speed-of-sound parametrization (see Tews et al. 2018). (These models were recently used by Capano et al. 2020 to obtain constraints on neutron star radii.) Chiral effective field theory is a systematic framework for low-energy hadronic interactions. For low densities, the theory describes matter using nucleons and pions, where the interactions are expanded in powers of momenta and all the relevant operators in strong interactions are included (Weinberg 1990, 1991; van Kolck 1994; Epelbaum, Hammer & Meißner 2009; Machleidt & Entem 2011). One then uses quantum Monte Carlo methods to solve the many-body Schrödinger equation to obtain an equation of state (Hebeler & Schwenk 2010; Krüger et al. 2013; Carlson et al. 2015; Tews et al. 2018). This approach is expected to describe matter well up to between one to two times nuclear saturation density. Tews et al. (2018) extended the equations of state to higher densities using a speed-of-sound parametrization to ensure that causality was not violated.

We consider a selection of models for the pressure–density relation [supplemented by the Douchin & Haensel (2001) table for the low-density regions ($\varepsilon \leq 1 \times 10^6\,\mathrm{g\,cm^{-3}}$)] and subject the stars to thermal pressure perturbations (as described in Section 4.2). We choose this mechanism since it produced the largest mountains from the examples we considered. The results are shown in Fig. 3.

It should be noted that there are observational and theoretical constraints on the mass and radius of neutron stars. From observations, it is apparent that the true nuclear-matter equation of state must be able to support $2\,\mathrm{M}_\odot$ neutron stars (Antoniadis et al. 2013). Additionally, there are recent constraints on the radius from NICER: PSR J0030+0451, with mass $M = 1.34\,\mathrm{M}_\odot$, was measured to have $11.52 \lesssim R/\mathrm{km} \lesssim 13.85$ (Riley et al. 2019) and PSR J0740+6620, with mass $M = 2.08\,\mathrm{M}_\odot$, was measured to have $11.41 \lesssim R/\mathrm{km} \lesssim 13.69$ (Riley et al. 2021). There have also been studies combining observations and theory to constrain the radius of a canonical $M = 1.4\,\mathrm{M}_\odot$ neutron star. Raaijmakers et al. (2020) used the NICER observation of PSR J0030+0451 along with GW170817 to obtain a constraint of $11.75 \lesssim R/\mathrm{km} \lesssim 13.5$. However, there is some degree of statistical uncertainty associated with this range and such constraints will need to be updated with future detections. Indeed, the study of Capano et al. (2020), that combined nuclear theory with observations of GW170817, found the contrasting (and more stringent) range $10.4 \lesssim R/\mathrm{km} \lesssim 11.9$ for an $M = 1.4\,\mathrm{M}_\odot$ neutron star. We add the mass limit of $M = 2\,\mathrm{M}_\odot$ and the radius ranges from the NICER measurements to the right-hand panel of Fig. 3. The majority of the equations of state that we consider support stars with $M = 2\,\mathrm{M}_\odot$. To give some indication of the accepted range of equations of state in the mass–radius diagram, we shade the region between models 833 and 1436, which (roughly) satisfy the observational constraints. In order to give context for some of the most constrained upper limits from

gravitational-wave data, we show the deformation constraint for PSR J0711–6830 of $\epsilon < 8.3 \times 10^{-9}$ in the left-hand panel (Abbott et al. 2020b).

In the left-hand panel of Fig. 3, we show the maximum deformations due to thermal pressure perturbations for the different equations of state. It is perhaps surprising to observe that there is a range of approximately two orders of magnitude across all the models. Thus, these mountain calculations are quite sensitive to the equation of state. However, as indicated by the shaded region of Fig. 3, the range of maximum deformations is narrower when we consider recent observational constraints on the equation of state.

One can also see that there is a relationship between the radius, R, of a star with a given mass, M, and the maximum deformation it supports. This should not be surprising, since equations of state that produce stars with larger radii will also have thicker crusts that can support larger deformations.

6 CONCLUSIONS

There is hope on the horizon that we will soon detect gravitational waves from rotating neutron stars for the very first time. Indeed, there are continued efforts to improve the data-analysis techniques (see, e.g., Dergachev & Papa 2020, 2021; Beheshtipour & Papa 2021; Steltner et al. 2021; Zhang et al. 2021), along with plans in development for third-generation gravitational-wave detectors to be constructed in the (hopefully) not-too-distant future (Maggiore et al. 2020). It is therefore meaningful to ask what may be the largest mountain neutron star crusts can support. Furthermore, such an answer could provide some helpful context in understanding the spin distribution of observed pulsars.

In our previous paper (Gittins et al. 2021), we surveyed previous maximum-mountain calculations and found that there were issues relating to boundary conditions that must be satisfied for realistic neutron stars. In particular, the usual approach to calculating maximum neutron star mountains of Ushomirsky et al. (2000) assumes a strain field that violates continuity of the traction. We introduced a new scheme for calculating mountains that gives one full control of the boundary conditions at the cost of requiring a knowledge of the deforming force that sources the mountains. However, it is unclear what this force should be. In reality, the force is related to the formation history of the star, which may involve complex mechanisms like quakes and accretion from a companion. Therefore, in order to get a handle on the force, evolutionary calculations that consider the history of neutron stars will be necessary. It should be noted that such calculations would need to be ambitious in order to take into account the physics that may be important in the evolution of the crust, such as cooling, freezing, spin-down, magnetic fields, and cracking (to name but a few mechanisms).

In this study, we generalized the scheme of Gittins et al. (2021) to relativity. We considered three examples for the deforming force and found the most promising results for thermal pressure perturbations. In constructing relativistic stellar models with a realistic equation of state, we noted that the size of the mountains was suppressed (in some cases, quite significantly). This is generally due to two factors: (i) using relativistic gravity and (ii) the shear modulus of the crust is weaker at points than the simple model used in Gittins et al. (2021). For most of the examples we examined, the crust yielded first at the top, where the shear modulus is the weakest. These results also point towards the necessity of evolutionary calculations in making progress on mountain calculations. This is evident from the role the deforming force plays in how large the mountains can be.

We have also demonstrated how the mountains are sensitive to the pressure–density relationship for nuclear matter, suggesting a range of uncertainty about an order of magnitude for a variety of equations of state that satisfy current observational constraints on the mass and radius. For this analysis, we considered a subset of equations of state from chiral effective field theory, that all obey causality, and subjected the stars to thermal pressure perturbations.

We made an effort to build a consistent neutron star model, based on the BSk24 equation of state (Pearson et al. 2018). However, our treatment of the crust is still somewhat simplistic: we assume that the crust behaves like an elastic solid up to some breaking strain, at which it yields and all the strain is subsequently released. As discussed by Gittins et al. (2021), a possible solution to constructing larger mountains than the ones we have been able to obtain perhaps lies in plasticity. Plastic solids behave elastically up to some strain and, beyond that strain, deform in such a way that they retain some of the strain. It is perhaps likely that neutron star crusts exhibit some of this behaviour. Suppose a neutron star crust is modelled as an ideal plastic. It is then deformed up to its elastic yield limit at a point in the crust and the strain saturates. Even if the force is increased, the strain stays the same. One could then continue to apply forces to the crust in order to build as large a mountain as possible. This may connect real neutron stars to the maximally strained configuration imposed in Ushomirsky et al. (2000). At present, this is speculation, even though there have been some interesting discussions of plasticity in neutron star crusts (Smoluchowski & Welch 1970; Jones 2003; Chugunov & Horowitz 2010). This idea certainly seems worthy of future studies.

ACKNOWLEDGEMENTS

NA is thankful for financial support from STFC via Grant No. ST/R00045X/1. The authors are especially grateful to I. Tews for supplying the chiral effective-field-theory equations of state.

DATA AVAILABILITY

Additional data underlying this article will be shared on reasonable request to the corresponding author.

REFERENCES

Aasi J. et al., 2013, Phys. Rev. D, 87, 042001
Aasi J. et al., 2014, ApJ, 785, 119
Aasi J. et al., 2015a, Phys. Rev. D, 91, 022004
Aasi J. et al., 2015b, Phys. Rev. D, 91, 062008
Abadie J. et al., 2011a, Phys. Rev. D, 83, 042001
Abadie J. et al., 2011b, ApJ, 737, 93
Abadie J. et al., 2012, Phys. Rev. D, 85, 022001
Abbott B. et al., 2004, Phys. Rev. D, 69, 082004
Abbott B. et al., 2005a, Phys. Rev. D, 72, 102004
Abbott B. et al., 2005b, Phys. Rev. Lett., 94, 181103
Abbott B. et al., 2007a, Phys. Rev. D, 76, 042001
Abbott B. et al., 2007b, Phys. Rev. D, 76, 082001
Abbott B. et al., 2008a, Phys. Rev. D, 77, 022001
Abbott B. et al., 2008b, ApJ, 683, L45
Abbott B. et al., 2009, Phys. Rev. D, 79, 022001
Abbott B. P. et al., 2010, ApJ, 713, 671
Abbott B. P. et al., 2016, Phys. Rev. D, 94, 042002
Abbott B. P. et al., 2017a, Phys. Rev. D, 95, 122003
Abbott B. P. et al., 2017b, Phys. Rev. D, 96, 062002
Abbott B. P. et al., 2017c, Phys. Rev. D, 96, 122006
Abbott B. P. et al., 2017d, Phys. Rev. Lett., 119, 161101
Abbott B. P. et al., 2017e, ApJ, 839, 12
Abbott B. P. et al., 2017f, ApJ, 847, 47
Abbott B. P. et al., 2018a, Phys. Rev. D, 97, 102003
Abbott B. P. et al., 2018b, Phys. Rev. Lett., 120, 031104
Abbott B. P. et al., 2019a, Phys. Rev. D, 99, 122002
Abbott B. P. et al., 2019b, Phys. Rev. D, 100, 024004
Abbott B. P. et al., 2019c, Phys. Rev. D, 100, 122002
Abbott B. P. et al., 2019d, ApJ, 879, 10
Abbott B. P. et al., 2020a, ApJ, 892, L3
Abbott R. et al., 2020b, ApJ, 902, L21
Abbott R. et al., 2021, ApJ, 913, L27
Andersson N., Kokkotas K. D., Stergioulas N., 1999, ApJ, 516, 307
Andersson N., Haskell B., Comer G. L., Samuelsson L., 2019, Class. Quantum Gravity, 36, 105004
Antoniadis J. et al., 2013, Science, 340, 448
Baiko D. A., Chugunov A. I., 2018, MNRAS, 480, 5511
Beheshtipour B., Papa M. A., 2021, Phys. Rev. D, 103, 064027
Bildsten L., 1998, ApJ, 501, L89
Binnington T., Poisson E., 2009, Phys. Rev. D, 80, 084018
Capano C. D. et al., 2020, Nat. Astron., 4, 625
Carlson J., Gandolfi S., Pederiva F., Pieper S. C., Schiavilla R., Schmidt K. E., Wiringa R. B., 2015, Rev. Mod. Phys., 87, 1067
Chugunov A. I., Horowitz C. J., 2010, MNRAS, 407, L54
Ciolfi R., Ferrari V., Gualtieri L., 2010, MNRAS, 406, 2540
Damour T., Nagar A., 2009, Phys. Rev. D, 80, 084035
Dergachev V., Papa M. A., 2020, Phys. Rev. Lett., 125, 171101
Dergachev V., Papa M. A., 2021, Phys. Rev. D, 103, 063019
Douchin F., Haensel P., 2001, A&A, 380, 151
Epelbaum E., Hammer H. W., Meißner U.-G., 2009, Rev. Mod. Phys., 81, 1773
Finn L. S., 1990, MNRAS, 245, 82
Frieben J., Rezzolla L., 2012, MNRAS, 427, 3406
Friedman J. L., Schutz B. F., 1978, ApJ, 221, 937
Gittins F., Andersson N., 2019, MNRAS, 488, 99
Gittins F., Andersson N., Pereira J. P., 2020, Phys. Rev. D, 101, 103025
Gittins F., Andersson N., Jones D. I., 2021, MNRAS, 500, 5570
Goriely S., Chamel N., Pearson J. M., 2013, Phys. Rev. C, 88, 024308
Gralla S. E., 2018, Class. Quantum Gravity, 35, 085002
Haskell B., Jones D. I., Andersson N., 2006, MNRAS, 373, 1423
Hebeler K., Schwenk A., 2010, Phys. Rev. C, 82, 014314
Hinderer T., 2008, ApJ, 677, 1216
Hinderer T., Lackey B. D., Lang R. N., Read J. S., 2010, Phys. Rev. D, 81, 123016
Horowitz C. J., Kadau K., 2009, Phys. Rev. Lett., 102, 191102
Ioka K., Sasaki M., 2004, ApJ, 600, 296
Johnson-McDaniel N. K., Owen B. J., 2013, Phys. Rev. D, 88, 044004
Jones P. B., 2003, ApJ, 595, 342
Krüger T., Tews I., Hebeler K., Schwenk A., 2013, Phys. Rev. C, 88, 025802
Machleidt R., Entem D. R., 2011, Phys. Rep., 503, 1

Maggiore M. et al., 2020, J. Cosmol. Astropart. Phys., 2020, 050
Ogata S., Ichimaru S., 1990, Phys. Rev. A, 42, 4867
Patruno A., Haskell B., Andersson N., 2017, ApJ, 850, 106
Pearson J. M., Chamel N., Potekhin A. Y., Fantina A. F., Ducoin C., Dutta A. K., Goriely S., 2018, MNRAS, 481, 2994
Penner A. J., Andersson N., Samuelsson L., Hawke I., Jones D. I., 2011, Phys. Rev. D, 84, 103006
Pereira J. P., Bejger M., Andersson N., Gittins F., 2020, ApJ, 895, 28
Raaijmakers G. et al., 2020, ApJ, 893, L21
Regge T., Wheeler J. A., 1957, Phys. Rev., 108, 1063
Riley T. E. et al., 2019, ApJ, 887, L21
Riley T. E. et al., 2021, preprint (arXiv:2105.06980)
Smoluchowski R., Welch D. O., 1970, Phys. Rev. Lett., 24, 1191
Steltner B. et al., 2021, ApJ, 909, 79
Tews I., Carlson J., Gandolfi S., Reddy S., 2018, ApJ, 860, 149
Thorne K. S., 1980, Rev. Mod. Phys., 52, 299
Ushomirsky G., Cutler C., Bildsten L., 2000, MNRAS, 319, 902
van Kolck U., 1994, Phys. Rev. C, 49, 2932
Wang M., Audi G., Kondev F. G., Huang W. J., Naimi S., Xu X., 2017, Chin. Phys. C, 41, 030003
Weinberg S., 1990, Phys. Lett. B, 251, 288
Weinberg S., 1991, Nucl. Phys. B, 363, 3
Woan G., Pitkin M. D., Haskell B., Jones D. I., Lasky P. D., 2018, ApJ, 863, L40
Yoshida S., Kiuchi K., Shibata M., 2012, Phys. Rev. D, 86, 044012
Zhang Y., Papa M. A., Krishnan B., Watts A. L., 2021, ApJ, 906, L14

This paper has been typeset from a TEX/LATEX file prepared by the author.